

# A Thermodynamic Model for the Prediction of Mild Steel Corrosion Products in an Aqueous Hydrogen Sulfide Environment

Jing Ning,\* Yougui Zheng,\* Bruce Brown,\* David Young,\* and Srdjan Nešić<sup>‡,\*</sup>

## ABSTRACT

*In the present study, a comprehensive thermodynamic model, depicted by Pourbaix diagrams, was developed with the relatively narrow focus on corrosion of mild steel in oil and gas field conditions. This thermodynamic model focuses on predicting the formation of metastable or stable corrosion products in sour environments at elevated temperature up to 250°C, which includes mackinawite (FeS), greigite (Fe<sub>3</sub>S<sub>4</sub>), the pyrrhotite group (Fe<sub>1-x</sub>S, x = 0 to 0.17), and pyrite (FeS<sub>2</sub>). The model is based on theoretical thermodynamic calculations and data found in the open literature. The appearance of Pourbaix diagram is significantly affected by temperature. Long-term corrosion experiments at two different temperature (25°C and 80°C) were conducted to investigate the corrosion product stability predictions made by the Pourbaix diagrams. The equilibrium state predicted in the Pourbaix diagrams was compared with the quasi-equilibrium state attained in the long-term experiments. To this end, the surface pH, bulk pH, ferrous ion concentration in solution, and corrosion potential were all monitored throughout the experiments. The morphology and composition of corrosion products formed on the mild steel sample surface was analyzed using scanning electron microscopy and x-ray diffraction. It was observed that the experimental results generally agreed with the predictions made by the Pourbaix diagrams.*

**KEY WORDS:** hydrogen sulfide, H<sub>2</sub>S corrosion, iron sulfide, polymorphous, Pourbaix diagram, thermodynamic

Submitted for publication: November 18, 2014. Revised and accepted: May 2, 2015. Preprint available online: May 3, 2015. <http://dx.doi.org/10.5006/1566>.

<sup>‡</sup> Corresponding author. E-mail: nesic@ohio.edu.

\* Institute for Corrosion and Multiphase Technology, Ohio University, 342 West State Street, Athens, OH 45701.

## INTRODUCTION

Although H<sub>2</sub>S corrosion of mild steel has been studied for over 60 y, the mechanisms of uniform H<sub>2</sub>S corrosion have been better understood in the recent decade.<sup>1-5</sup> It is broadly agreed that the formation of an iron sulfide layer on the steel surface plays an essential role in the corrosion of the steel underneath. Many researchers<sup>6-8</sup> have reported a significant decrease in corrosion rate after the formation of the protective iron sulfide layer in a sour environment. Hence, in order to make an accurate prediction of the corrosion rate, the mechanisms related to the formation of the iron sulfide layer need to be better understood.

In many cases of published modeling work, only the mackinawite layer (the initial corrosion product in sour environments) has been considered for a reason of simplicity.<sup>3-4</sup> However, polymorphous iron sulfides such as greigite, pyrrhotite, troilite, and pyrite have been found in facilities containing H<sub>2</sub>S in the oil and gas industry.<sup>9</sup> Furthermore, these iron sulfides are reported to either retard or promote<sup>10</sup> corrosion as a result of the different physicochemical nature associated with each one. Menendez, et al.,<sup>11</sup> studied the impact of different phases of iron sulfide deposits, such as mackinawite, pyrrhotite, and troilite, on initiation of pitting corrosion in a highly sour environment. It was found that severe localized attack was associated with mackinawite deposits, but not with pyrrhotite and troilite deposits. Therefore, there is a need to investigate the influences of iron sulfide polymorphism

on corrosion and incorporate this effect into simulation models.

However, the formation and transformation of the polymorphous iron sulfides are complex processes, which are affected by both thermodynamics and kinetics. A Pourbaix diagram, also known as potential-pH stability diagram, has been frequently used to map out corrosion product stability from a thermodynamic perspective. Accordingly, one can make extremely valuable inferences for practical purposes from a Pourbaix diagram, including developing corrosion mitigation strategies, defining cathodic protection conditions, and designing critical corrosion tests with higher efficiency.<sup>12</sup> In fact, one can find a number of thermodynamic models, in the form of Pourbaix diagrams for sour systems, in both the open literature and proprietary commercial packages.<sup>13-16</sup> However, significant discrepancies among these models have been found, which are attributed to variations in the choice of the underlying thermodynamic data, selection of chemical species and chemical reactions considered, and different assumptions adopted for calculations (for example: open system vs. closed system), all making it harder for corrosion engineers to use them with confidence. Thus, in the present work development of calculations underlying Pourbaix diagrams for mild steel corrosion in H<sub>2</sub>S environments is shown, covering typical conditions seen in the oil and gas industry. The diagrams are based on open literature data and are presented in a simple way, making it easier for corrosion engineers to understand and interpret them.

## CONSTRUCTION OF POURBAIX DIAGRAMS FOR AN H<sub>2</sub>S-H<sub>2</sub>O-Fe SYSTEM

It is noteworthy that some important assumptions were made here when constructing Pourbaix diagrams, as will be shown. Only ideal behavior of aqueous solutions has been considered in the present work, for reasons of simplicity. Also, only an open system is considered in this study, meaning that the partial pressure of H<sub>2</sub>S is considered to be constant across the whole pH and potential range. This is in contrast with most of the Pourbaix diagrams found in the open literature<sup>15-19</sup> for similar conditions, which were constructed for a closed system, where the total amount of sulfur species is considered to be constant. This leads to a different water speciation particularly in the high pH range, and a different appearance of the Pourbaix diagram.

### Theoretical Thermodynamic Background

Because thermodynamic properties are significantly sensitive to temperature, but relatively insensitive to pressure,<sup>12</sup> the effect of increasing pressure on thermodynamic properties is neglected in this study. Therefore, the Gibbs energy of formation for species

at elevated temperature is calculated following Equation (1), which is a temperature-dependent function of Gibbs energy of formation at 298.15 K,  $G_{298.15}^{\circ}$ , heat capacity,  $C_p$ , and standard M entropy at 298.15 K,  $S_{298.15}^{\circ}$ .

$$G_{T,P}^{\circ} = G_{298.15}^{\circ} + \int_{298.15}^T C_p dT - T \int_{298.15}^T \frac{C_p}{T} dT - (T - 298.15) \times S_{298.15}^{\circ} \quad (1)$$

The Gibbs energy of formation and standard M entropy for most species at reference temperature can be found in the open literature (see Table 1). The heat capacity of various species can be predicted as a function of temperature by using Equation (2):

$$C_p = a + bT + cT^{-2} + dT^2 + eT^{-0.5} \text{ J/mol/K} \quad (2)$$

where a, b, c, d, and e are constants that can be obtained from literature.

It should be noted that the Gibbs energy for the electron is also considered in this work. Because the Gibbs energy of formation for aqueous H<sup>+</sup> is defined to be 0 at any temperature,<sup>20-21</sup> the Gibbs energy for the electron is considered to be half of Gibbs energy for hydrogen gas, shown in Equation (3):<sup>20,22</sup>

$$G(e) = 0.5G(H_2) \quad (3)$$

### Thermodynamic Data

The standard Gibbs energy at 25°C,  $G_{298.15}^{\circ}$ , for all species considered in the H<sub>2</sub>S-H<sub>2</sub>O-Fe system has been compiled and presented in the previous work.<sup>23</sup> In the present work, two other thermodynamic properties,  $S_{298.15}^{\circ}$  and  $C_p$ , are needed for all of the species considered in the H<sub>2</sub>S-H<sub>2</sub>O-Fe system. For most of the species, thermodynamic data are mainly collected from literature. However, thermodynamic properties for mackinawite and greigite cannot be found in literature because these two compounds are not thermodynamically stable, thereby making experimental measurements hard to perform. Therefore, the heat capacities and entropies for these two species are estimated by following certain principles.

*Thermodynamic Data Compiled from Literature* — Thermodynamic data for the aqueous, solid, and gaseous species considered here were compiled from various sources. For some species, the thermodynamic data compiled from various sources were consistent. If H<sub>2</sub>S<sub>(g)</sub> is taken as an example, Figure 1(a) shows the data for  $S_{298.15}^{\circ}$  from various sources<sup>24-32</sup> are in good agreement. The average value is 205.7±0.1 J/mol/K. Heat capacity for H<sub>2</sub>S<sub>(g)</sub> was predicted using five different models,<sup>24,26-28,32</sup> as shown in Figure 1(b). Within the temperature range of 298 K to 1,800 K, the agreement between the different models was exceptionally good. The data for  $S_{298.15}^{\circ}$  and  $C_p$  for H<sub>2</sub>S<sub>(g)</sub> from Knacke, et al.,<sup>26</sup> were selected for further use in the present study.

**TABLE 1**  
Thermodynamic Data of the Species Considered for H<sub>2</sub>S-H<sub>2</sub>O-Fe System

Species	G <sup>o</sup> <sub>298.15</sub> (kJ/mol)	S <sup>o</sup> <sub>298.15</sub> (J/mol/K)	C <sub>p</sub> = a + bT + cT <sup>-2</sup> + dT <sup>2</sup> (J/mol/K)				Valid Tem. (K)	Ref.
			a	b×10 <sup>3</sup>	c×10 <sup>-6</sup>	d×10 <sup>6</sup>		
H <sup>+</sup> (aq)	0	0	0	0	0	0	all	21
H <sub>2</sub> S (g)	-33.329	205.757	34.911	10.686	-0.448	0	2,980-2,000	26
H <sub>2</sub> O (l)	-237.141	69.948	20.335	109.198	2.033	0	298-500	26
H <sub>2</sub> (g)	0	130.679	26.882	3.586	0.105	0	298-3,000	26
O <sub>2</sub> (g)	0	205.146	29.154	6.477	-0.184	-1.017	298-3,000	26
Fe (s)	0	27.28	28.18	-7.32	-0.29	25	298-800	24
Fe <sup>2+</sup> (aq)	-91.5	-105.6	-2	0	0	0	Unknown	33, 36
Fe <sup>3+</sup> (aq)	-17.24	-276.94	-143	0	0	0	Unknown	33, 36
Fe <sub>2</sub> O <sub>3</sub> (s) <sup>(A)</sup>	-743.523	87.4	-838.61	-2,343.4	0	605.19	298-950	27
Fe <sub>3</sub> O <sub>4</sub> (s) <sup>(B)</sup>	-1,017.438	146.14	2,659.1	-2,521.53	20.734	1,368	298-900	33
Fe(OH) <sub>2</sub> (s)	-491.969	87.864	116.064	8.648	-2.874	0	298-1,358	26
FeS (s) (mackinawite)	-100.07	56.52	44.685	19.037	-0.289	0		Estimated
Fe <sub>3</sub> S <sub>4</sub> (s) (greigite)	-311.88	182.13	143.344	76.567	0	0		Estimated
FeS (s) (pyrrhotite)	-101.95	60.291	-0.502	170.707	0	0	298-411	26
FeS <sub>2</sub> (s) (pyrite)	-160.06	52.928	68.952	141	-0.987	0	298-1,016	26

(A) C<sub>p(Fe<sub>2</sub>O<sub>3</sub>)</sub> = a + bT + cT<sup>-2</sup> + dT<sup>2</sup> + fT<sup>0.5</sup> + gT<sup>-1</sup> (J/mol/K), where f = 86,525 and g = 27,821.

(B) C<sub>p(Fe<sub>3</sub>O<sub>4</sub>)</sub> = a + bT + cT<sup>-2</sup> + dT<sup>2</sup> + eT<sup>-0.5</sup> (J/mol/K), where e = -36,460.

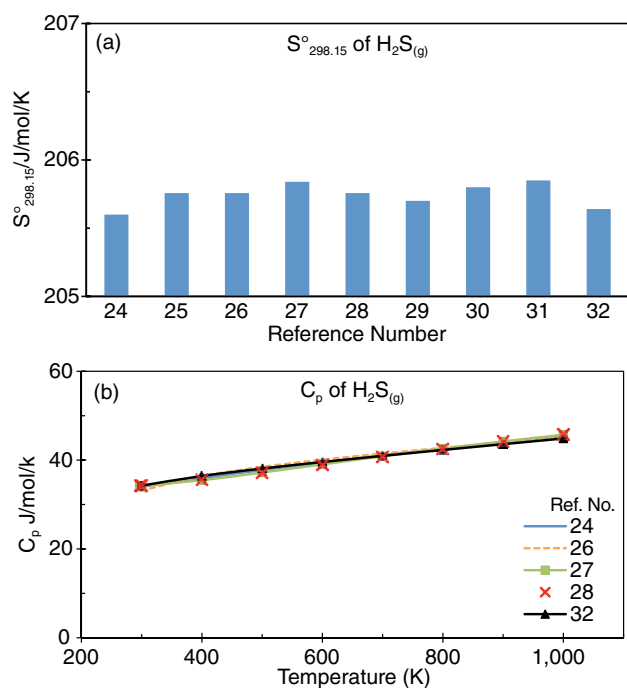


**FIGURE 1.** The collection of data for H<sub>2</sub>S(g) from various sources: (a) standard M entropy at 25°C, S<sup>o</sup><sub>298.15</sub>, (b) heat capacity, C<sub>p</sub>.

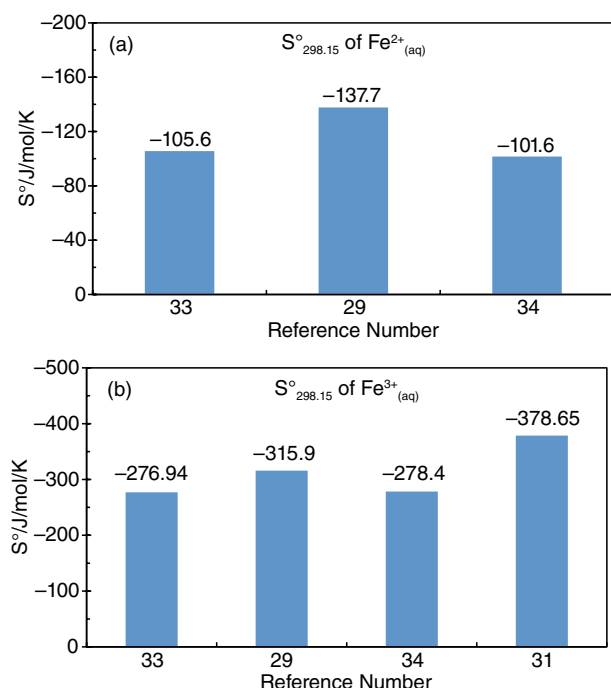


**FIGURE 2.** The collection of data of S<sup>o</sup><sub>298.15</sub> for (a) Fe<sup>2+</sup><sub>(aq)</sub>, (b) Fe<sup>3+</sup><sub>(aq)</sub> from various sources.

However, the thermodynamic data for some other species had a significant variation between different sources, for instance S<sup>o</sup><sub>298.15</sub> data for aqueous Fe<sup>2+</sup> and Fe<sup>3+</sup> species, as illustrated in Figure 2. The S<sup>o</sup><sub>298.15</sub> data for these two species calculated by Beverskog, et al.,<sup>33</sup> were adopted for further use in the present study. Moreover, only one source<sup>35-36</sup> was found for the C<sub>p</sub> for aqueous Fe<sup>2+</sup> and Fe<sup>3+</sup>, and was therefore used in the

present study even if the valid temperature range was not defined.

In addition, it should be emphasized that both stoichiometric troilite (FeS) and pyrrhotite (Fe<sub>0.877</sub>S) were considered to be part of the pyrrhotite group (Fe<sub>1-x</sub>S, x = 0 to 0.17) in the present work because of the similarity found for their thermodynamic data. Figure 3 summarizes the heat capacity and the stan-

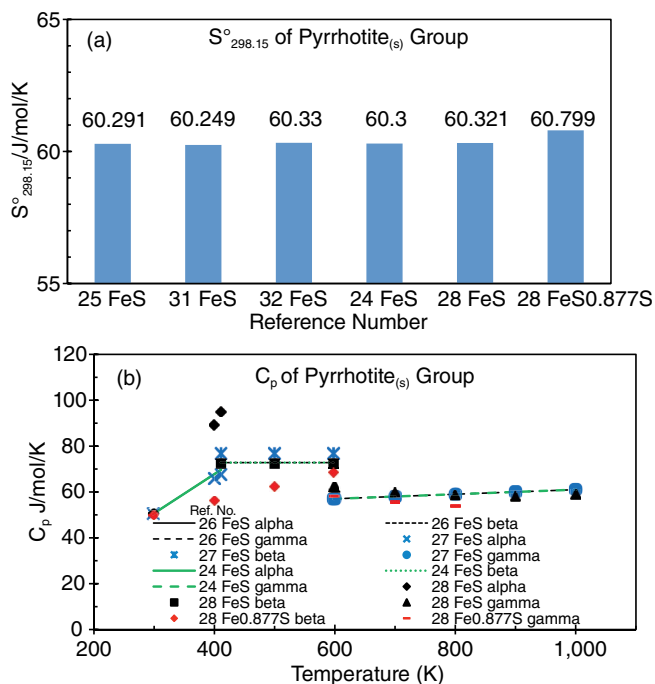


FIGURE 3. The collection of data for pyrrhotite<sub>(s)</sub> group from various sources: (a)  $S^{\circ}_{298.15}$ ; (b)  $C_p$ .

standard M entropy for both troilite and pyrrhotite. Figure 3(a) shows that the standard M entropy for troilite and pyrrhotite are very close, with an average value of  $60.38 \pm 0.21$  J/mol/K. It is acknowledged that the phase transition of troilite and pyrrhotite (i.e., alpha, beta, and gamma) affects the heat capacity; hence, different heat capacities were used for each phase in the present study. Figure 3(b) illustrates that the heat capacity values for troilite and pyrrhotite phases obtained from various sources agree with each other very well. As a result, the heat capacity and the standard M entropy for troilite reported by Knacke, et al.,<sup>26</sup> were taken for pyrrhotite group  $Fe_{1-x}S$  ( $x = 0$  to 0.17).

The compiled data for  $S^{\circ}_{298.15}$  and  $C_p$  for the following species:  $H_2O_{(l)}$ ,  $H_{2(g)}$ ,  $O_{2(g)}$ ,  $Fe_{(s)}$ ,  $Fe^{2+}_{(aq)}$ ,  $Fe^{3+}_{(aq)}$ ,  $Fe_2O_{3(s)}$ ,  $Fe_3O_{4(s)}$ ,  $Fe(OH)_{2(s)}$ ,  $FeS_{(s)}$  (the pyrrhotite group), and  $FeS_{2(s)}$  (pyrite), are summarized in Table 1.

**Thermodynamic Data by Estimation** — The heat capacity for some species, such as mackinawite and greigite, could not be found in the open literature and had to be estimated. These were estimated on the basis of data available for other metal sulfides, such as Cr, Mn, Co, Ni, Cu, and Ru, as a result of the good agreement between data found for their heat capacities, as illustrated in Figures 4(a) through (c). The heat capacity for NiS was adopted as the heat capacity for mackinawite. Similarly, the heat capacity for  $Co_3S_4$  was used for greigite.

The entropies for mackinawite and greigite were estimated by using the following two rules. The first one was proposed by Gronvold and Westrum,<sup>37</sup> which is to estimate the entropy of a compound by combin-

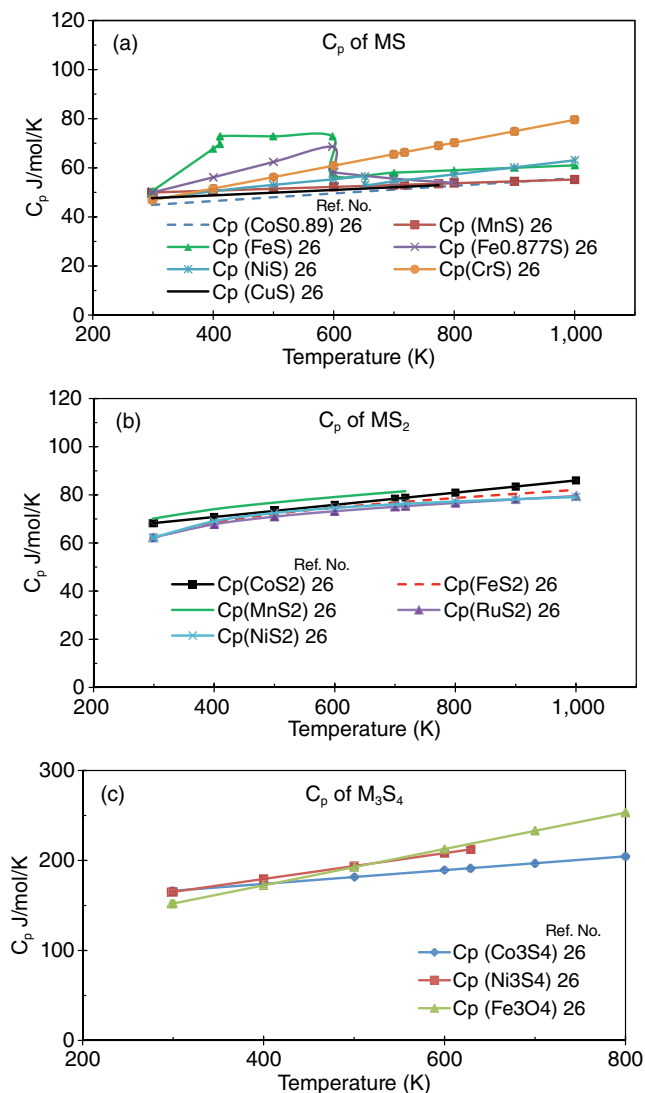


FIGURE 4. Heat capacity of metal sulfides: (a) MS, (b)  $MS_2$ , (c)  $M_3S_4$ .

ing the cationic entropy contribution and anionic entropy contribution. Therefore, the entropies for metal sulfides were calculated as the sum of entropy of chemical elements in accordance with the chemical formula. In light of this estimation rule, the entropies for mackinawite and greigite were estimated to be 56.52 J/mol/K and 182.13 J/mol/K, respectively. Another methodology of estimating entropy<sup>38</sup> was tested in the present work, for verification purposes. The rule is to sum up the average entropies for iron (27.3 J/mol/K) and sulfur (31.92 J/mol/K) according to the chemical formula of a compound. The resultant entropy for mackinawite was estimated to be 59 J/mol/K and for greigite was 208.9 J/mol/K. Overall, similar entropies for mackinawite and greigite were estimated by using these two methodologies; therefore, it was concluded that either could be used with confidence. In the end, the entropies for mackinawite and greigite were estimated by using the first methodology.

## Pourbaix Diagrams

The Pourbaix diagrams for an  $\text{H}_2\text{S}$ - $\text{H}_2\text{O}$ -Fe system were constructed in a stepwise fashion, starting from a simple system moving to a more complicated system. The chemical species, electrochemical reactions, and chemical reactions considered for the  $\text{H}_2\text{O}$ -Fe system and the  $\text{H}_2\text{S}$ - $\text{H}_2\text{O}$ -Fe system are listed in the previous publication.<sup>23</sup>

It is noteworthy that the focus of this work was on conditions typical for corrosion of mild steel pipelines transporting oil and gas. Therefore, the range of pH and corrosion potentials considered in this work is narrower than typically seen in textbook cases. In the present study, the usual pH range is between pH 3 and pH 7, while the corrosion potentials are between  $-0.5$  V and  $-0.3$  V vs. standard hydrogen reference electrode. Hence, the species appearing beyond pH 12 and potentials above 1.0 V vs. standard hydrogen reference electrode were not considered here. Examples are  $\text{Fe}(\text{OH})_3$ ,  $\text{HFeO}_2^-$ , and the polysulfide species (i.e.,  $\text{S}_n^{2-}$ ) present at high pH values, or the  $\text{SO}_4^{2-}$  and elemental sulfur appearing at higher potentials. For Pourbaix diagrams covering this broader range of pH and potential, one can refer to open literature, such as the work of Anderko and Shuler,<sup>15</sup> Anderko, et al.,<sup>16</sup> Biernat and Robbins,<sup>17</sup> Macdonald and Syrett,<sup>18</sup> and Chen, et al.<sup>19</sup>

**Pourbaix Diagram for an  $\text{H}_2\text{O}$ -Fe System** — As a starting point, a well-known Pourbaix diagram for an  $\text{H}_2\text{O}$ -Fe system generated at a specific condition is shown in Figure 5. The areas of “ $\text{Fe}(\text{OH})_2$ ,” “ $\text{Fe}_2\text{O}_3$ ,” and “ $\text{Fe}_3\text{O}_4$ ” indicate the formation of a certain corrosion product layer, but do not indicate how this layer affects corrosion. The protectiveness of the formed layer depends on its adherence to the steel surface, thickness, porosity, tortuosity, and physicochemical properties, such as crystal structure and defects, which are related to the kinetics of formation.<sup>39</sup>

**Pourbaix Diagram for an  $\text{H}_2\text{S}$ - $\text{H}_2\text{O}$ -Fe System** — To construct Pourbaix diagrams for an  $\text{H}_2\text{S}$ - $\text{H}_2\text{O}$ -Fe system, the reactions of the formation of mackinawite ( $\text{FeS}$ ), greigite ( $\text{Fe}_3\text{S}_4$ ), the pyrrhotite group ( $\text{FeS}$ ), and pyrite ( $\text{FeS}_2$ ) are incorporated into the Pourbaix diagram for the  $\text{H}_2\text{O}$ -Fe system. Consequently, Pourbaix diagrams for the  $\text{H}_2\text{S}$ - $\text{H}_2\text{O}$ -Fe system with the addition of mackinawite, greigite, the pyrrhotite group, and pyrite are shown in Figures 6(a), (b), (c), and (d), respectively, and are indicated by the black solid lines. Only pyrrhotite and pyrite exist in the Pourbaix diagram that considers all four iron sulfides in Figure 6(d), suggesting that these two phases of iron sulfide are the final and thermodynamically stable iron sulfides.

## Parameter Study

The effects of increasing temperature, ferrous ion concentration in solution, and  $\text{H}_2\text{S}$  partial pressure on features of Pourbaix diagrams for  $\text{H}_2\text{S}$ - $\text{H}_2\text{O}$ -Fe system are described next.

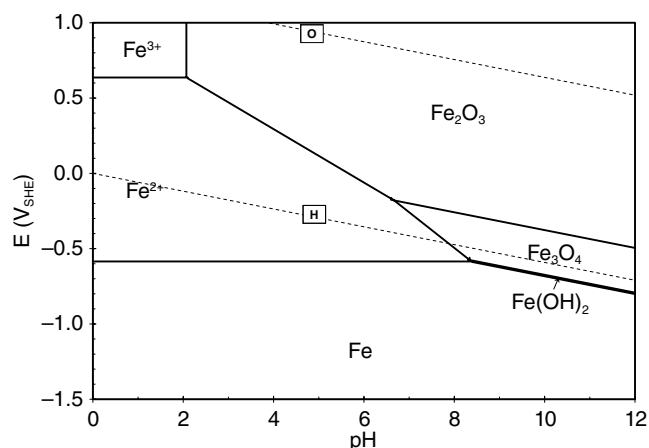


**FIGURE 5.** Pourbaix diagram for  $\text{H}_2\text{O}$ -Fe system ( $T = 25^\circ\text{C}$ ,  $[\text{Fe}^{2+}] = 10$  ppm,  $[\text{Fe}^{3+}] = 10^{-6}$  mol/L,  $p\text{H}_2 = p\text{O}_2 = 100$  kPa).

**Effect of Temperature** — Because thermodynamic properties are highly sensitive to temperature, the Pourbaix diagrams for  $\text{H}_2\text{S}$ - $\text{H}_2\text{O}$ -Fe system generated at  $25^\circ\text{C}$ ,  $80^\circ\text{C}$ ,  $150^\circ\text{C}$ , and  $250^\circ\text{C}$  are presented in Figure 6 using the colored lines. In order to compare Pourbaix diagrams among different temperature in a reasonable way, the dissolved  $\text{H}_2\text{S}$  concentration in aqueous solution was maintained at a constant level ( $9.4 \times 10^{-3}$  mol/L) during the construction of the series of Pourbaix diagrams.

A gradual shift of the stability areas for formed solids to lower pH and to more negative potential with increasing temperature is clear in Figure 6. This indicates that higher temperature is more thermodynamically favorable for the formation of a corrosion product layer, such as iron sulfides and hematite, possibly retarding the corrosion rate of the steel underneath. Abayarathna, et al.,<sup>40</sup> conducted steel corrosion tests with a continuous purge of pure  $\text{H}_2\text{S}$  gas into brine at  $50^\circ\text{C}$ ,  $70^\circ\text{C}$ , and  $90^\circ\text{C}$  for 2 d of exposure. The results show that the final corrosion rate at  $90^\circ\text{C}$  was much lower than that at  $50^\circ\text{C}$  as a result of the formation of the more protective iron sulfide layer at  $90^\circ\text{C}$ .

In addition, the type of the corrosion product formed was also affected by changing temperature. In Figures 6(b) and (c), greigite is predicted to be the main corrosion product at  $25^\circ\text{C}$  through  $200^\circ\text{C}$ , but not at  $250^\circ\text{C}$ . At  $250^\circ\text{C}$ , greigite is completely replaced by hematite because hematite is more stable than greigite at  $250^\circ\text{C}$ .

**Effect of  $\text{H}_2\text{S}$  Partial Pressure** — Variation of another significant factor, partial pressure of  $\text{H}_2\text{S}$ , is also considered here. The Pourbaix diagrams are developed for partial pressure of  $\text{H}_2\text{S}$  at 0.01 kPa (0.0001 bar, 100 ppm at atmospheric pressure), 10 kPa (0.1 bar), 100 kPa (1 bar), and 1,000 kPa (10 bar) and shown in Figure 7.

A major effect of increasing partial pressure of  $\text{H}_2\text{S}$  on the features of Pourbaix diagrams is the extension of the corrosion product layer stability region,

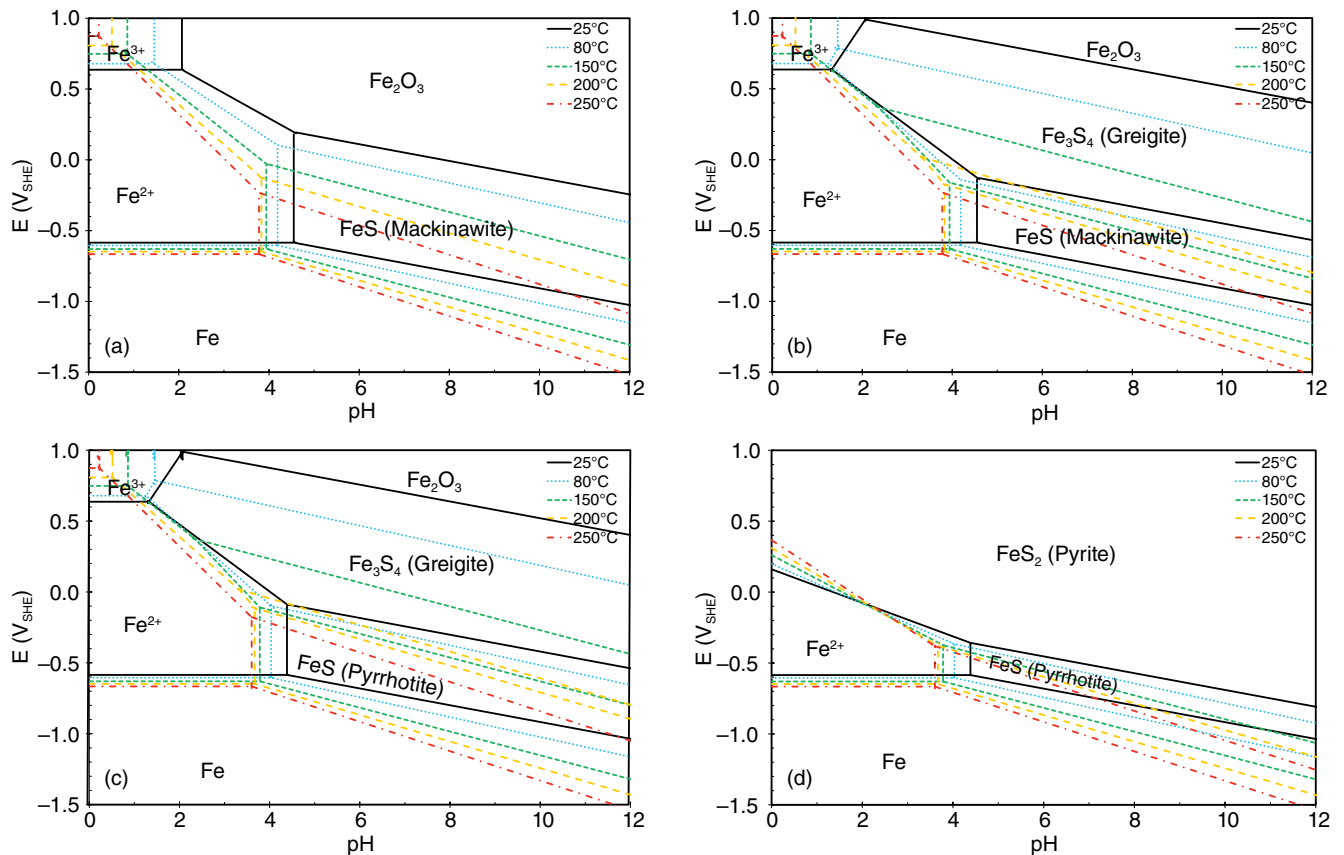


**FIGURE 6.** Pourbaix diagrams for  $\text{H}_2\text{S}$ - $\text{H}_2\text{O}$ - $\text{Fe}$  system showing step changes in temperature up to  $250^\circ\text{C}$  ( $T = 25^\circ\text{C}$  to  $250^\circ\text{C}$ ,  $[\text{H}_2\text{S}]_{\text{aq}} = 9.4 \times 10^{-3} \text{ M}$ ,  $[\text{Fe}^{2+}] = 10 \text{ ppm}$ ,  $[\text{Fe}^{3+}] = 10^{-6} \text{ M}$ ): (a) mackinawite, (b) mackinawite/greigite, (c) mackinawite/greigite/pyrrhotite, (d) mackinawite/greigite/pyrrhotite/pyrite.

particularly that of iron sulfide. Because mackinawite usually forms as the initial and main corrosion product in  $\text{H}_2\text{S}$  corrosion and provides some protectiveness, the understanding of conditions leading to establishment of mackinawite layer is critical to short-term corrosion studies. Figure 7(a) shows that the increase in  $\text{H}_2\text{S}$  partial pressure from 0.01 kPa to 1,000 kPa (0.0001 bar to 10 bar) dramatically pushes the boundary of mackinawite formation region from pH 6.0 to pH 3.3, revealing the formation of mackinawite layer is more thermodynamically favored at higher  $\text{H}_2\text{S}$  partial pressure.

Furthermore,  $\text{Fe}_3\text{O}_4$  is seen in the presence of trace amounts of  $\text{H}_2\text{S}$  (0.01 kPa, 0.0001 bar) but is replaced by iron sulfides at higher concentrations of  $\text{H}_2\text{S}$ , as shown in Figures 7(a) through (c).

**Effect of Ferrous Ion Concentration** — The concentration of ferrous ions in solution directly affects the saturation value for iron sulfide. Sun, et al.,<sup>41</sup> concluded that the effect of ferrous ion concentration on  $\text{H}_2\text{S}$  corrosion rate is negligible because the solubility of iron sulfide is so small that supersaturation for iron sulfide can be easily reached.

Figure 8 shows a series of Pourbaix diagrams developed with 1 ppm, 10 ppm, and 100 ppm ferrous

ion concentration. Notice that the “ $\text{Fe}^{2+}$ ” area shrinks with increasing ferrous ion concentration, which is considered to be an indication that bare steel corrosion is less likely. However, the increase in size of the iron sulfide stability area does not necessarily guarantee better protectiveness of the formed iron sulfide layer, which is more related to the kinetics aspects.

## EXPERIMENTAL VERIFICATION OF CONSTRUCTED POURBAIX DIAGRAMS

A comprehensive thermodynamic model for the  $\text{H}_2\text{S}$ - $\text{H}_2\text{O}$ - $\text{Fe}$  system, in the form of Pourbaix diagrams, was described in the previous section with the relatively narrow focus on predicting corrosion products for environments similar to those found in the oil and gas fields. After the establishment of the theoretical model, verification of the Pourbaix diagrams is required by performing experiments. It is notoriously difficult to verify Pourbaix diagrams because of a variety of theoretical and practical limitations.

First, thermodynamics is a science related to the equilibrium state defined by thermodynamic state variables, which are independent on the path and the history (time) of the system. To be more specific, for

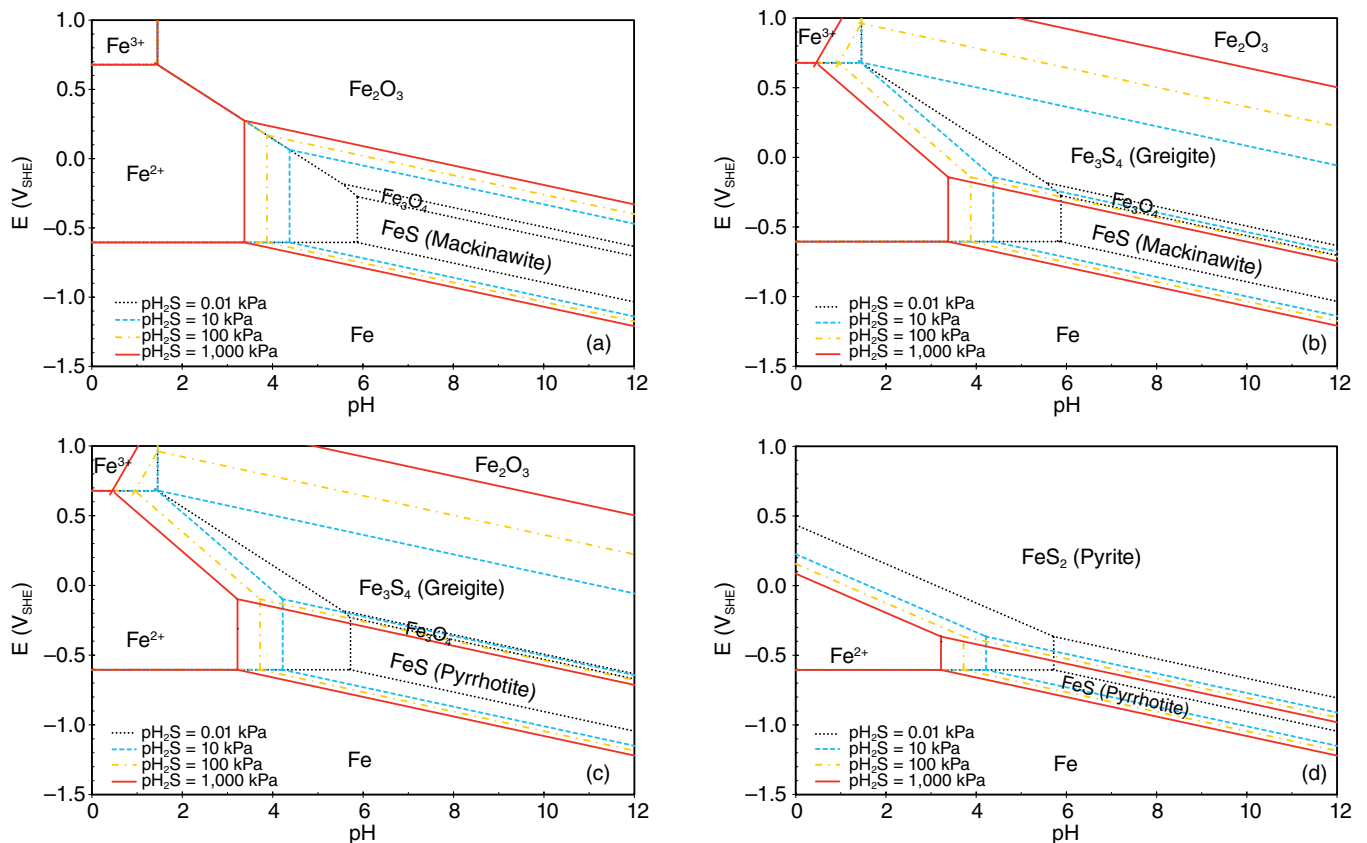


**FIGURE 7.** Pourbaix diagrams for  $H_2S$ - $H_2O$ -Fe system showing step changes in  $H_2S$  partial pressure ( $p_{H_2S} = 100$  ppm – 1,000 kPa,  $T = 80^\circ\text{C}$ ,  $[Fe^{2+}] = 10$  ppm,  $[Fe^{3+}] = 10^{-6}$  M): (a) mackinawite, (b) mackinawite/greigite, (c) mackinawite/greigite/pyrrhotite, (d) mackinawite/greigite/pyrrhotite/pyrite.

given conditions of pH and potential, a specific iron sulfide is predicted to form by the Pourbaix diagram, but how that iron sulfide forms and how long it takes to form are unknown. Considering the stabilities of four different kinds of iron sulfides makes this thermodynamic model more complex and harder to verify. Moreover, in reality, most systems are transient, which means they are not in thermodynamic equilibrium and are gradually changing over time. In the present study, two long-term corrosion tests at two different temperature ( $25^\circ\text{C}$  and  $80^\circ\text{C}$ ) were performed to test the corrosion product stability predictions by the Pourbaix diagrams, and especially to compare the equilibrium state (given by the line) in the Pourbaix diagram with the quasi-equilibrium state attained in long-term experiments.

In addition, there is another experimental challenge, and that is to accurately determine pH and ferrous ion concentration at the steel surface, which can be very different from those in the bulk. In the present work, a mesh capped flat pH probe<sup>42</sup> was used for improved estimation of surface pH. The measured ferrous ion concentration in the bulk solution in well-mixed conditions was used to approximate the surface ferrous ion concentration.

## Experimental

**Apparatus** — The experimental setup is depicted in Figure 9. Experiments were performed in a 2 L glass cell filled with 1 wt% NaCl electrolyte at atmospheric pressure. Square samples were suspended in the glass cell. One rotating cylinder electrode (RCE) sample was used as the working electrode to conduct electrochemical measurements, but was not rotated during the experiment. A platinum wire was used as the counter electrode. A saturated Ag/AgCl electrode connected to the cell externally through a Luggin capillary was used as the reference electrode. The open circuit potential (OCP) of the RCE electrode was monitored using a potentiostat. A magnetic stirring bar with 400 rpm stirring speed was used to mix the solution during the experiment. A mesh capped pH probe was used to measure surface pH at steel mesh surface and a regular pH probe was used to monitor bulk solution pH as well. The concentration of  $H_2S$  in the mixed  $H_2S/N_2$  gas was adjusted by using a gas rotameter and confirmed by a gas sample pump with  $H_2S$  detector tubes. Sodium hydroxide solution and a carbon scrubber were used to remove  $H_2S$  from the gas coming out of the glass cell.

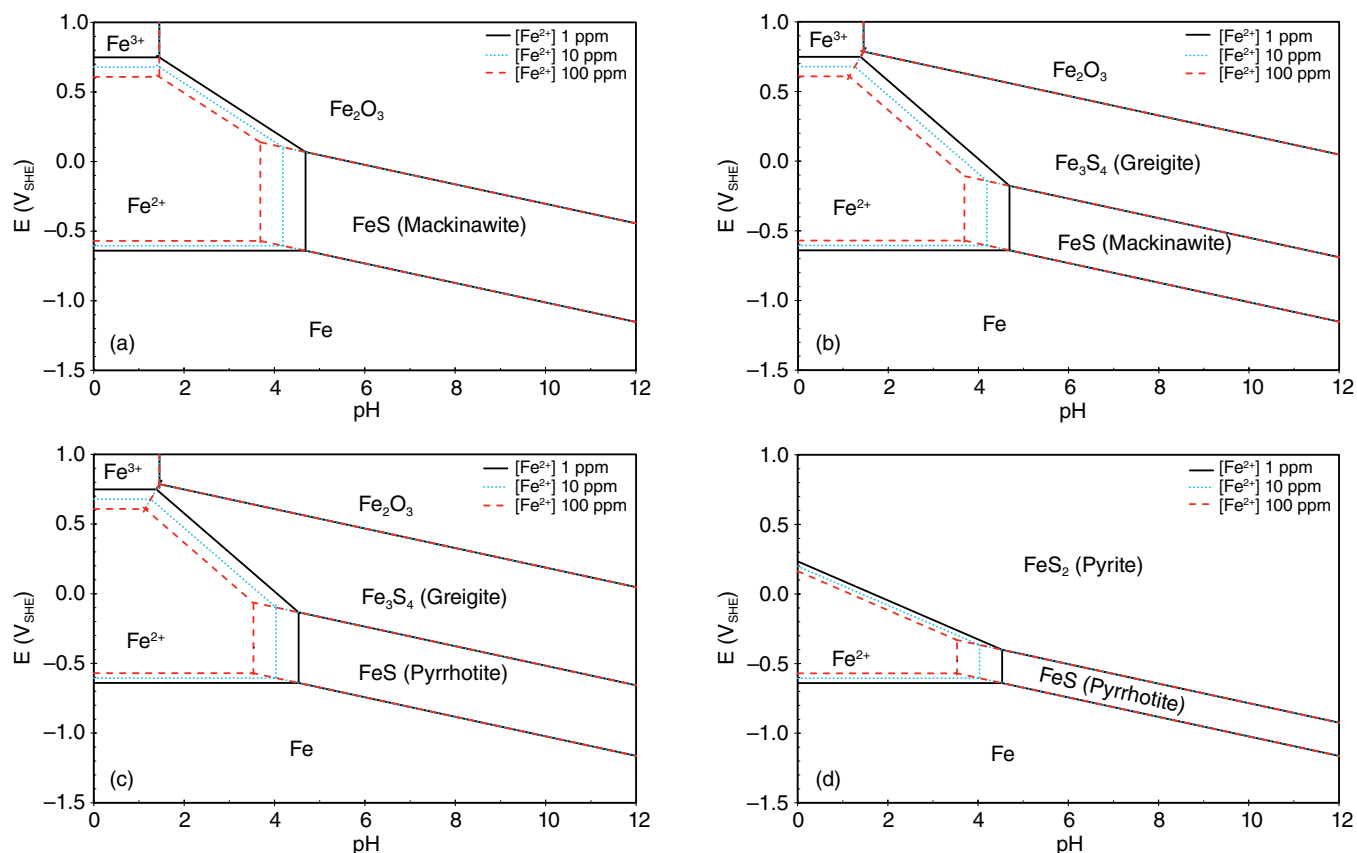


**FIGURE 8.** Pourbaix diagrams for  $H_2S$ - $H_2O$ -Fe system showing step changes in ferrous ion concentration ( $[Fe^{2+}] = 1$  ppm to 100 ppm,  $T = 80^\circ C$ ,  $p_{H_2S} = 24$  kPa,  $[Fe^{3+}] = 10^{-6}$  M): (a) mackinawite, (b) mackinawite/greigite, (c) mackinawite/greigite/pyrrhotite, (d) mackinawite/greigite/pyrrhotite/pyrite.



**FIGURE 9.** Experimental setup.

**Material** — The square samples with  $1.2\text{ cm} \times 1.2\text{ cm} \times 0.2\text{ cm}$  dimension and the RCE sample with an exposed area of  $5.4\text{ cm}^2$  were machined from American Petroleum Institute (API) 5L X65 carbon

steel. The chemical composition of the API 5L X65 carbon steel is presented in Table 2.

**Procedure** — The test matrix is shown in Table 3. The experiments were conducted with 10%  $H_2S$  in the gas phase at  $25^\circ C$  and  $80^\circ C$ , corresponding to a  $H_2S$  partial pressure of 9.7 kPa (0.097 bar) at  $25^\circ C$  and 5.3 kPa (0.053 bar) at  $80^\circ C$ . Prior to a test,  $N_2$  gas was purged into the electrolyte until saturation to deoxygenate the solution (typically more than 4 h). An  $H_2S$  and  $N_2$  premixed gas was then purged into the solution until the solution pH stabilized and was purged continuously throughout the experiment. Before positioning steel samples in the glass cell, the solution pH was adjusted to 6.0 by using deoxygenated NaOH solution. The RCE sample and square samples were finally polished with 600 grit sandpaper, then rinsed thoroughly with deionized (DI) water and isopropanol before immersion in solution. Corroded square samples were taken out for analysis at different points in time, rinsed with deoxygenated DI water and deoxygenated isopropanol, blown dry using  $N_2$ , and stored in a desiccator. Scanning electron microscope (SEM) imaging was used to detect the surface morphologies of the square samples. X-ray diffraction (XRD) was applied to determine which iron sulfides formed on

**TABLE 2**  
Chemical Composition of 5L X65 Carbon Steel Used in Experiment (wt%)

Cr	Mo	S	V	Si	C	Fe	Ni	Mn	P
0.14	0.16	0.009	0.047	0.26	0.13	Balance	0.36	1.16	0.009

the square samples. Both linear polarization resistance and weight loss methods were adopted for corrosion rate measurements. Approximately 10 mL of solution were drawn from the glass cell immediately before taking each steel specimen, filtered by using a 0.22  $\mu\text{m}$  syringe filter to remove any iron sulfide precipitate from the solution, and then taken for the measurement of ferrous ion concentration using a spectrophotometric method.

### Results and Discussion

**Verification of Pourbaix Diagram for  $\text{H}_2\text{S}$ - $\text{H}_2\text{O}$ - $\text{Fe}$  System at 25°C**— To verify the basis of this thermodynamic model, the first corrosion test was performed at 25°C. Figure 10(a) shows the surface pH, bulk pH, and the ferrous ion concentration in the bulk solution changing over time. One could observe that the surface pH was approximately 0.5 pH unit higher than the bulk pH in the initial 3 d, which reflects the rapid release of  $\text{Fe}^{2+}$  ions and consumption of hydrogen ions in the corrosion reaction. After 3 d, the surface pH became lower than the bulk pH, which was a result of the release of hydrogen ions (acidification) during precipitation of iron sulfide. Figure 10(b) shows that both corrosion rate and OCP had small changes in the first d and then were very stable through the 7 d of the experiment.

At the time each square sample was removed from the cell for the determination of corrosion product composition, a set of operational parameters was determined and used to define the “operational point” in the Pourbaix diagram. This included the values of OCP and surface pH, ferrous ion concentration,  $\text{H}_2\text{S}$  partial pressure, and temperature.

- Results After 1 Day of Exposure: Figures 11(a) and (b) show the surface morphologies of the sample after 1 d of exposure. A partially covered corrosion product layer was observed on the surface, and was

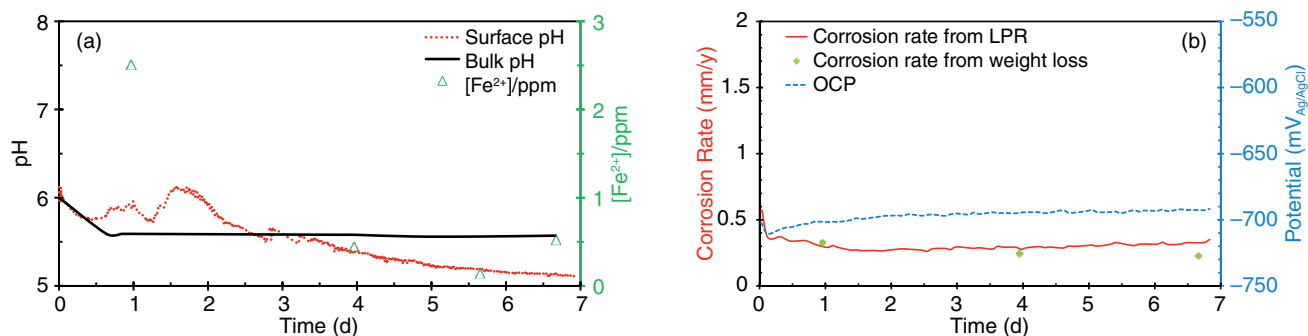
**TABLE 3**  
Test Matrix

Description	Parameter
Temperature	25°C, 80°C
Solution	1 wt% NaCl brine
Purge gas	10% $\text{H}_2\text{S}$ /balance $\text{N}_2$
$\text{H}_2\text{S}$ partial pressure	9.7 kPa (25°C), 5.3 kPa (80°C)
Stirring speed	400 rpm
Material	API 5L X65

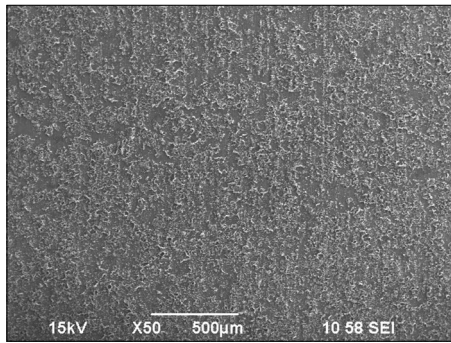
identified to be only mackinawite by XRD, as shown in Figure 11(c).

Figure 12 shows the Pourbaix diagram constructed at this experimental condition, which considers only mackinawite corrosion product and excludes other polymorphous iron sulfides. According to the intersection of potential and surface pH from measurement in Figure 12, mackinawite was predicted to form on the steel surface, which was detected in the experiment as well.

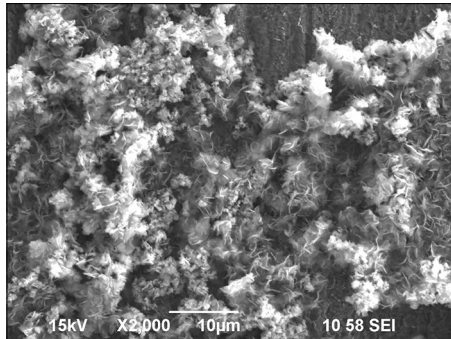
Moreover, the operational point is a little to the right of the equilibrium line between mackinawite and aqueous  $\text{Fe}^{2+}$ , which indicates a slight supersaturation for mackinawite (a nonequilibrium state) at this condition. This statement is quantified by calculating the saturation value for mackinawite, using Equation (4), which gives  $S = 20$ . This could be an experimental artifact resulting from the errors made in estimating the surface pH and ferrous ion concentration, but it could also be true—indicating that kinetics of mackinawite formation at 25°C lag behind the corrosion process. If the latter is true, as time progresses, one would expect the saturation value to decrease and the intersection of potential and surface pH to be closer to the equilibrium line, which is exactly what was seen in the results collected after 4 d and 7 d of exposure.



**FIGURE 10.** (a) Measured bulk pH, surface pH, and  $[\text{Fe}^{2+}]$ , (b) corrosion rate and OCP during experiment at 25°C.



(a)



(b)

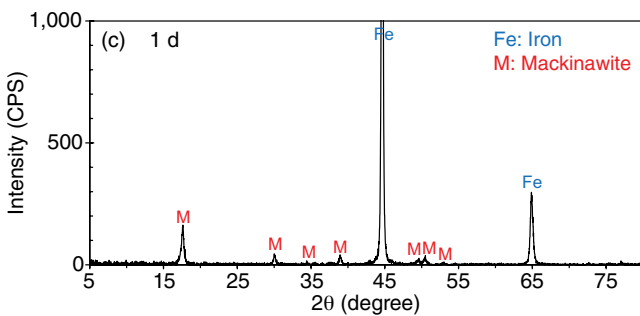


FIGURE 11. Corrosion product layer after 1 d of exposure at 25°C: (a) surface morphology with 100x magnification, (b) surface morphology with 2,000x magnification, (c) XRD pattern.

$$S_{\text{Mackinawite}} = \frac{c_{\text{Fe}^{2+}} \cdot c_{\text{HS}^-}}{K_{\text{sp},2} \cdot c_{\text{H}^+}} \quad (4)$$

• Results After 4 Days of Exposure: Figure 13 presents the surface morphology and compositional analysis of the corrosion product layer on the steel surface after 4 d of exposure. A steel surface covered with more corrosion product layer is observed in Figure 13(a). SEM image at higher magnification (Figure 13[b]) showed this corrosion product to be in the form of “plates” and some slender needle-like clusters. XRD pattern in Figure 13(c) suggested the presence of mackinawite with a small amount of pyrrhotite.

According to the Pourbaix diagrams constructed at this experimental condition and shown in Figure 14, the expected corrosion products were mackinawite and pyrrhotite, which were both detected by XRD.

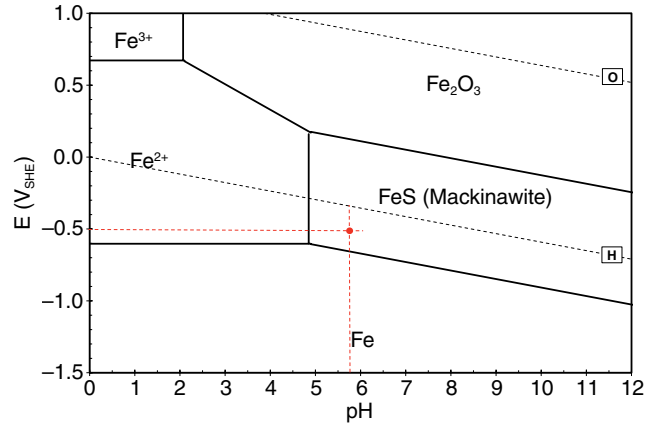
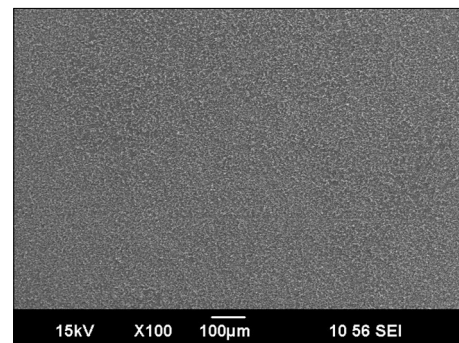
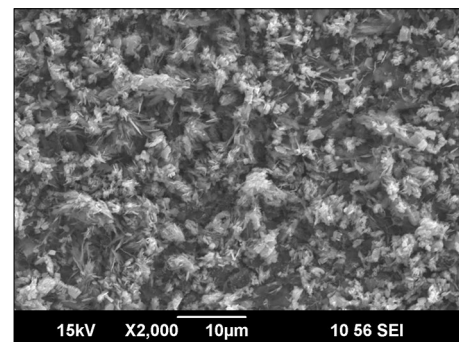


FIGURE 12. Verification of Pourbaix diagram after 1 d of exposure (Pourbaix diagram was generated at  $T = 25^\circ\text{C}$ ,  $p\text{H}_2\text{S} = 9.7 \text{ kPa}$ ,  $[\text{Fe}^{2+}] = 2.5 \text{ ppm}$ ,  $[\text{Fe}^{3+}] = 1.0 \times 10^{-6} \text{ M}$ ).



(a)



(b)

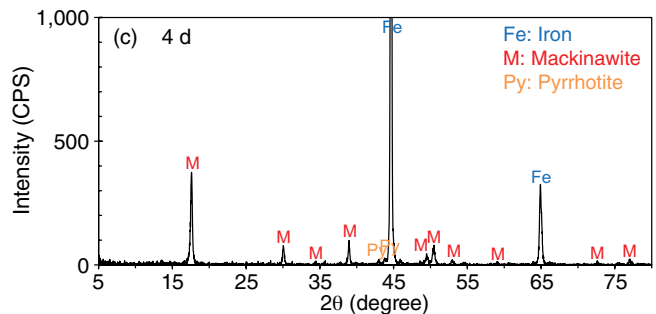
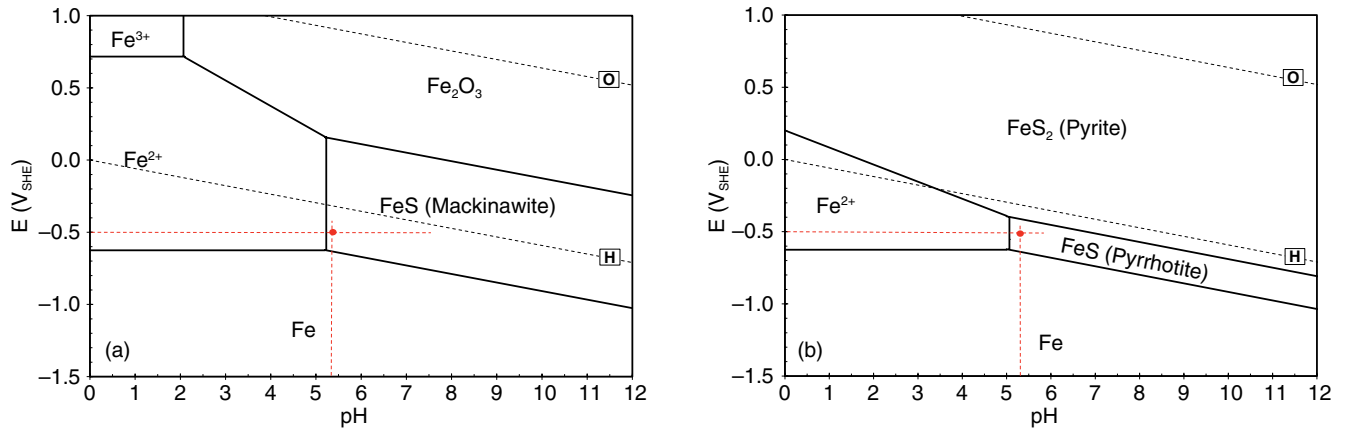


FIGURE 13. Corrosion product layer after 4 d of exposure at 25°C: (a) SEM image of surface morphology with 100x magnification, (b) SEM image of surface morphology with 2,000x magnification, (c) XRD pattern.



**FIGURE 14.** Verification of Pourbaix diagram after 4 d of exposure (Pourbaix diagram was generated at  $T = 25^\circ\text{C}$ ,  $p\text{H}_2\text{S} = 9.7 \text{ kPa}$ ,  $[\text{Fe}^{2+}] = 0.44 \text{ ppm}$ ,  $[\text{Fe}^{3+}] = 1.0 \times 10^{-6} \text{ M}$ ): (a) mackinawite, (b) mackinawite/greigite/pyrrhotite/pyrite.

The dominant corrosion product, mackinawite, is a thermodynamic metastable phase which forms first because of its faster kinetics. It will transform to a thermodynamically more stable phase, pyrrhotite or pyrite, over time. However, the time of this transformation cannot be depicted in the Pourbaix diagram, and two different Pourbaix diagrams are shown in Figure 14.

Furthermore, comparing with the previous results collected after 1 d of exposure, the operational point in Figure 14(a) was much closer to the equilibrium line for mackinawite, and the saturation value was 2. This implies that the system is approaching the equilibrium for formation of mackinawite. The operational point in the Pourbaix diagram showing pyrrhotite (Figure 14(b)) was further to the right of the equilibrium line, suggesting slower kinetics of formation.

- Results After 7 Days of Exposure: Figure 15 demonstrates the morphology and composition of corrosion product layer on the steel surface after corroding for 7 d. The SEM image with 100x magnification shows a fully covered steel surface. The SEM image with higher magnification presents a mixture of flaky crystals and needle-like clusters. Again, mackinawite and pyrrhotite were detected by XRD with mackinawite as the dominate polymorph.

Referring to the Pourbaix diagrams generated at this experimental condition (Figure 16), mackinawite and pyrrhotite were predicted as stable, which were also detected in the experiment.

In addition, the operational point is almost on the equilibrium line between mackinawite and ferrous ion in Figure 16(a), which indicates that after long-term exposure for 7 d, the system finally reached a state very close to the equilibrium between mackinawite precipitation and dissolution, which is here called quasi-equilibrium. The saturation value for mackinawite after 7 d of exposure was computed to be 0.7. The operational point in the Pourbaix diagram showing pyrrhotite given in Figure 16(b) is also closer

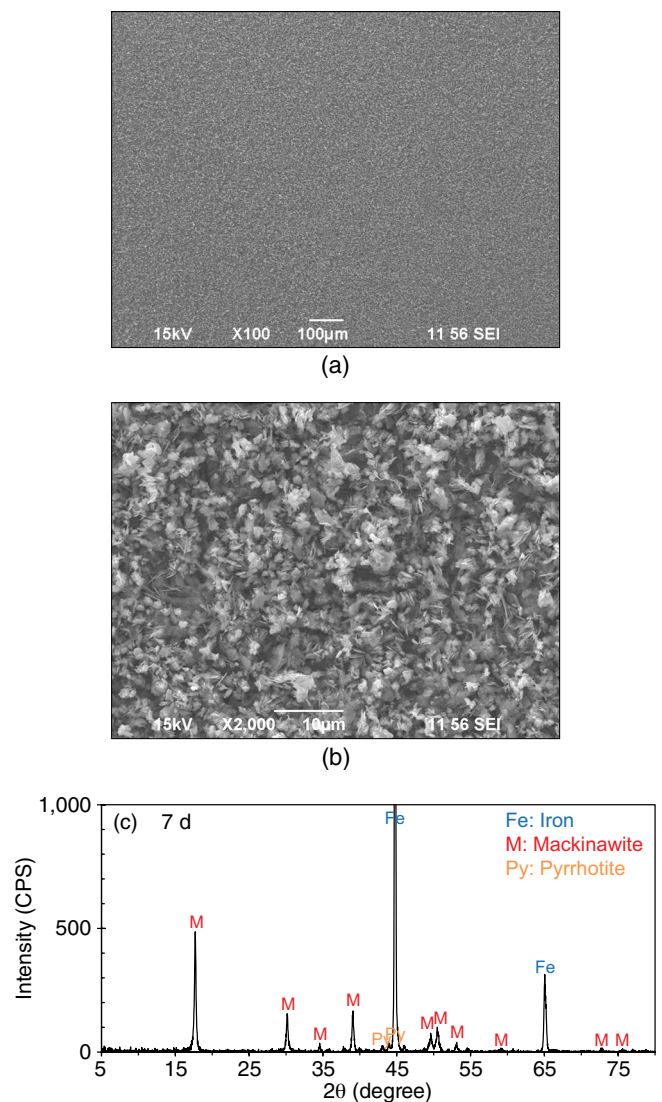


**FIGURE 15.** Corrosion product layer after 7 d of exposure at  $25^\circ\text{C}$ : (a) SEM image of surface morphology with 100x magnification, (b) SEM image of surface morphology with 2,000x magnification, (c) XRD pattern.

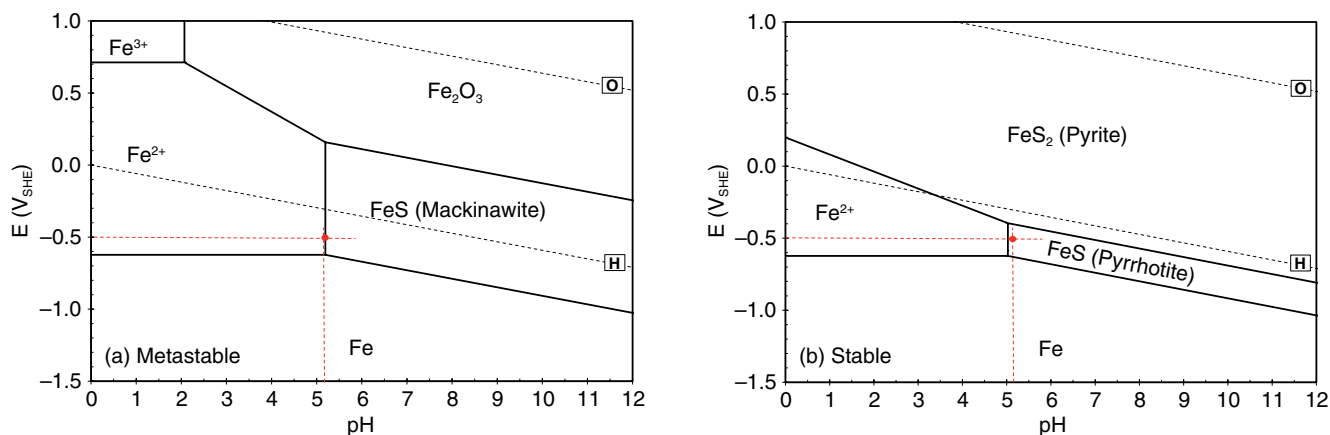


**FIGURE 16.** Verification of Pourbaix diagram after 7 d of exposure (Pourbaix diagram was generated at  $T = 25^{\circ}\text{C}$ ,  $\text{pH}_2\text{S} = 9.7 \text{ kPa}$ ,  $[\text{Fe}^{2+}] = 0.52 \text{ ppm}$ ,  $[\text{Fe}^{3+}] = 1.0 \times 10^{-6} \text{ M}$ ): (a) mackinawite, (b) mackinawite/greigite/pyrrhotite/pyrite.

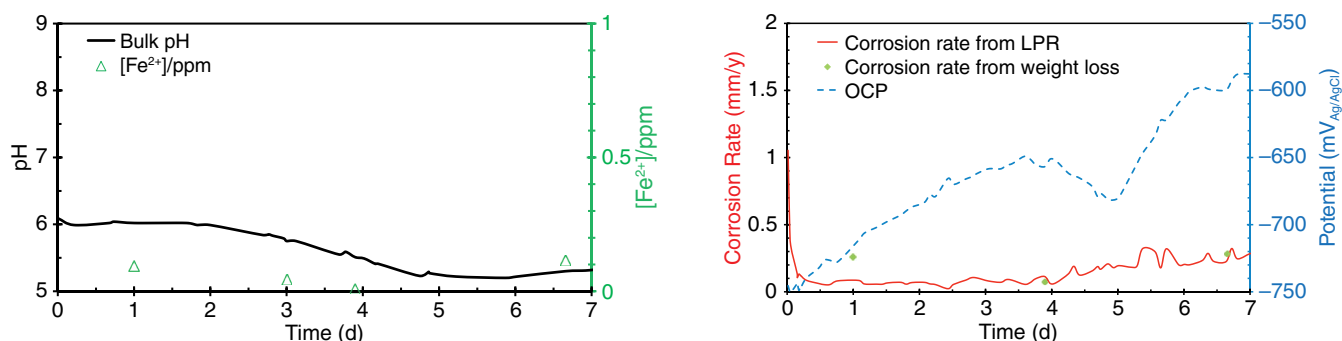


**FIGURE 17.** (a) Measured bulk pH and  $[\text{Fe}^{2+}]$ , (b) corrosion rate and OCP during experiment at  $80^{\circ}\text{C}$ .

to the equilibrium line, suggesting that the formation of pyrrhotite also approached equilibrium after 7 d of exposure at  $25^{\circ}\text{C}$ . The consistency of these results presents credible evidence in favor of the accuracy of the current thermodynamic model, at least for  $25^{\circ}\text{C}$ .

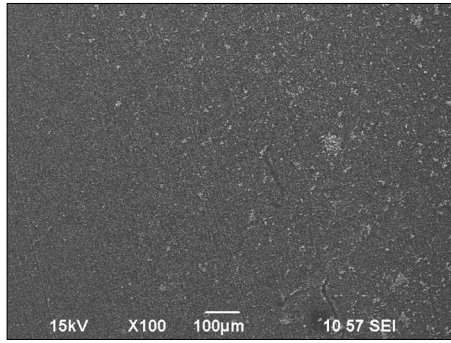
**Verification of Pourbaix Diagram for  $\text{H}_2\text{S}$ - $\text{H}_2\text{O}$ - $\text{Fe}$  System at  $80^{\circ}\text{C}$**  — It is known that increasing temperature facilitates the transformation of the metastable phases (mackinawite or greigite) into more stable phases (pyrrhotite or pyrite). Compared to the low temperature experiments presented earlier, different phases of iron sulfides should be detected in the high-temperature conditions. Moreover, increasing temperature also expedites the kinetics and the approach of the equilibrium state. Therefore, a second set of experiments at higher temperature,  $80^{\circ}\text{C}$ , were performed for verification.

Figure 17(a) shows the bulk pH monitored and  $[\text{Fe}^{2+}]$  measured through the experiment. Figure 17(b) demonstrates the evolution of OCP and corrosion rates during the test. The corrosion rate decreased from  $1.1 \text{ mm/y}$  to a stable value around  $0.07 \text{ mm/y}$  in the first 4 d, probably because of the formation of a protective mackinawite layer, but then increased gradually. A significant change in OCP was observed at the same time. This effect on the corrosion rate is

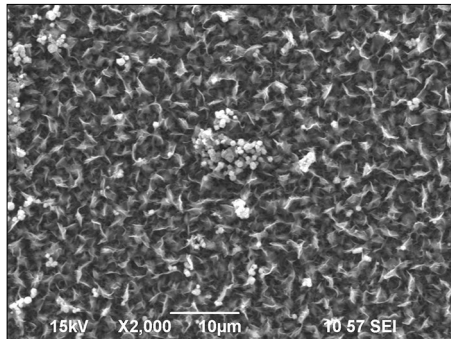
very interesting and could be the effect of other iron sulfide phases forming on the steel surface. However, a deeper analysis is currently under way and a full presentation exceeds the scope of the current paper.

- **Results After 1 Day of Exposure:** In Figure 18, the SEM images show a uniform corrosion product layer formed on the steel surface after 1 d of exposure, which was characterized to be only mackinawite by XRD. According to the Pourbaix diagram generated at experimental conditions after 1 d in Figure 19, the mackinawite corrosion product was predicted, which matches the experimental result. The operational point was to the right of the equilibrium line, indicating the system was in a nonequilibrium state for mackinawite formation after 1 d of exposure. The supersaturation value for mackinawite was computed to be 78, which suggests precipitation of mackinawite was not at the equilibrium state. Even if precipitation of mackinawite was accelerated at  $80^{\circ}\text{C}$ , the corrosion rate was as well, making it difficult to reach equilibrium after only 1 d of exposure.

- **Results After 4 Days of Exposure:** Figure 20 shows the surface morphologies and composition of the corrosion product layer on the sample surface after 4 d of exposure. Figure 20(b) shows some small cubic crystals on the corrosion product layer, which



(a)



(b)

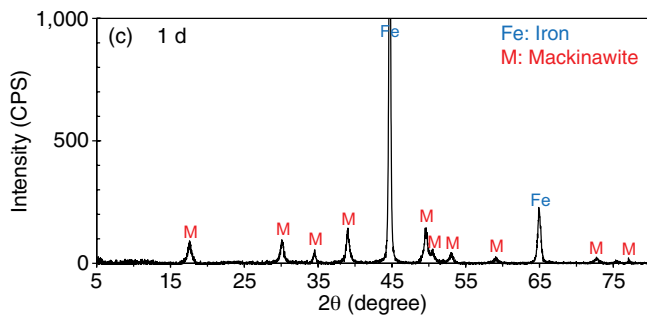


**FIGURE 18.** Corrosion product layer after 1 d of exposure at 80°C: (a) SEM image of surface morphology with 100x magnification, (b) SEM image of surface morphology with 2,000x magnification, (c) XRD pattern.

are suspected to be pyrite. From XRD patterns, beside mackinawite and pyrrhotite, a new iron sulfide phase was detected as pyrite, which never appeared in the previous experiment at 25°C. That is because pyrite is a thermodynamic stable phase whose formation is favored by the high temperature in this test. Table 4 gives the quantitative analysis of the formed corrosion products by following reference intensity ratio methodology. Mackinawite accounts for 34% and pyrite comprises 2.1% of the total detected layer on the sample surface.

The formation of pyrite was also predicted by the Pourbaix diagram generated according to experimental conditions after 4 d, as shown in Figure 21. From Figure 21(a), we can see that the operational point is very close to the boundary for mackinawite formation, which indicates the state of quasi-equilibrium for this

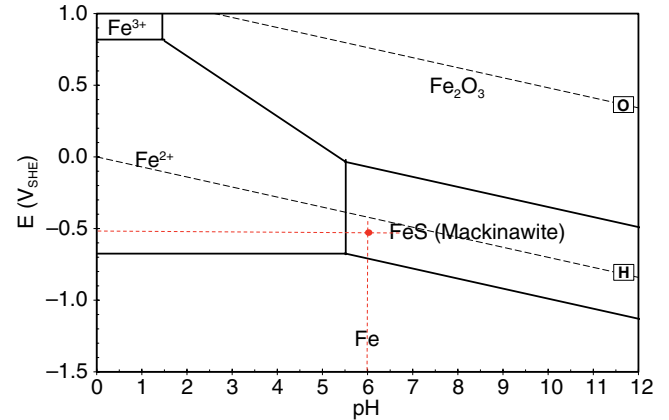
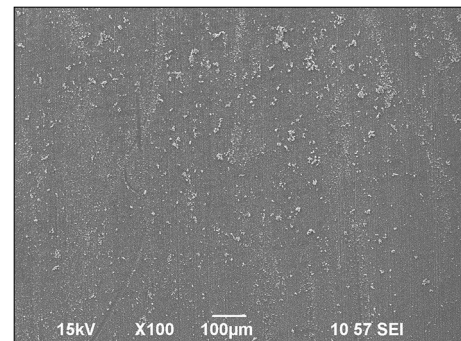
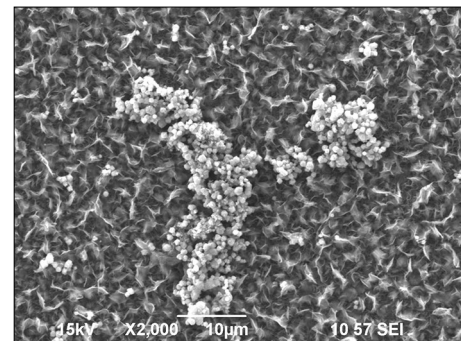


**FIGURE 19.** Verification of Pourbaix diagram after 1 d of exposure (Pourbaix diagram was generated at  $T = 80^\circ\text{C}$ ,  $p\text{H}_2\text{S} = 5.3 \text{ kPa}$ ,  $[\text{Fe}^{2+}] = 0.1 \text{ ppm}$ ,  $[\text{Fe}^{3+}] = 1.0 \times 10^{-6} \text{ M}$ ).



(a)



(b)

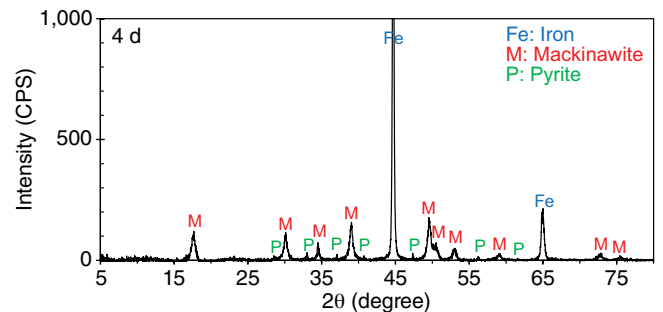


**FIGURE 20.** Corrosion product layer after 4 d of exposure at 80°C: (a) SEM image of surface morphology with 100x magnification, (b) SEM image of surface morphology with 2,000x magnification, (c) XRD pattern.

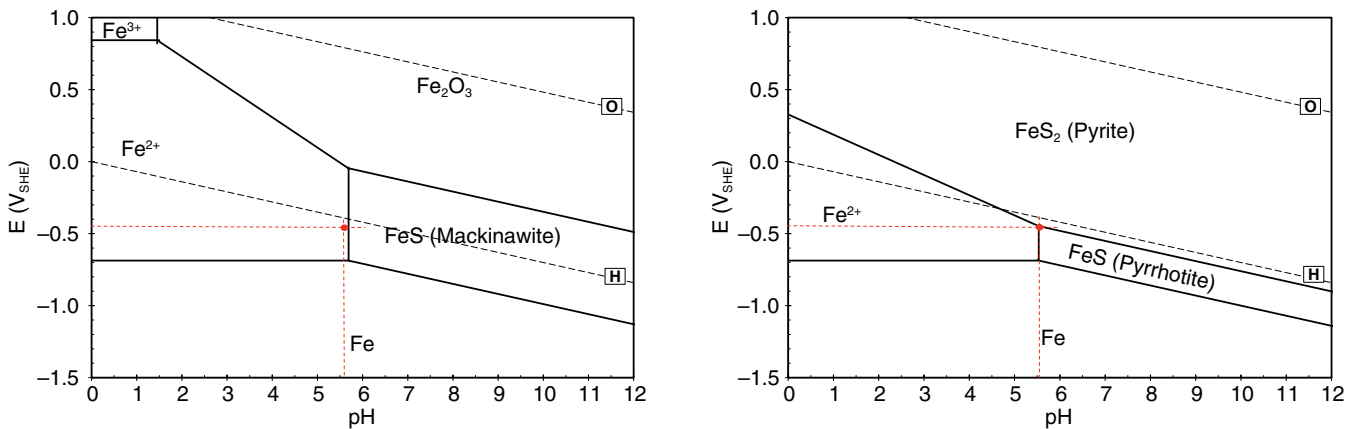
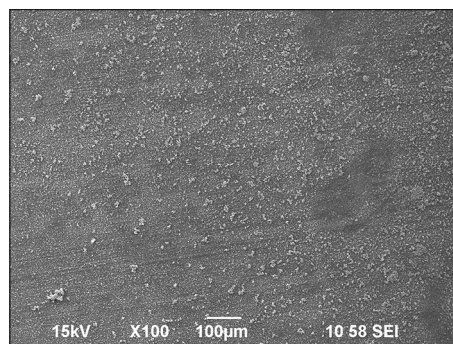
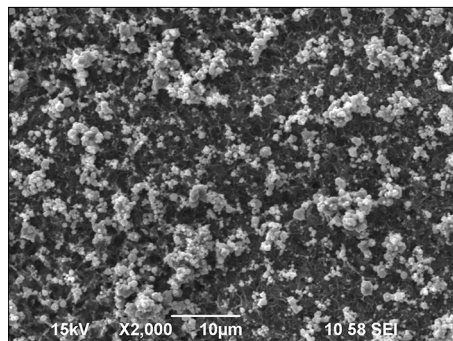


**FIGURE 21.** Verification of Pourbaix diagram after 4 d of exposure (Pourbaix diagram was generated at  $T = 80^{\circ}\text{C}$ ,  $p\text{H}_2\text{S} = 5.3 \text{ kPa}$ ,  $[\text{Fe}^{2+}] = 0.045 \text{ ppm}$ ,  $[\text{Fe}^{3+}] = 1.0 \times 10^{-6} \text{ M}$ ): (a) mackinawite, (b) mackinawite/greigite/pyrrhotite/pyrite.



(a)



(b)

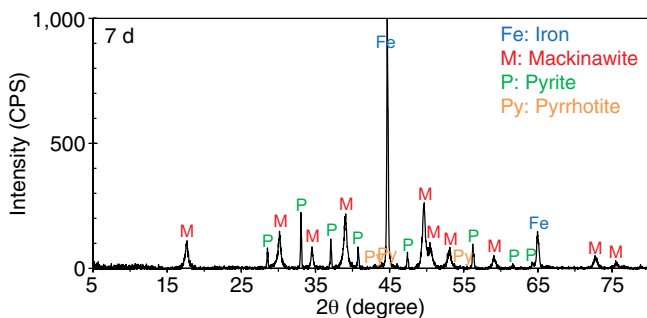


**FIGURE 22.** Corrosion product layer after 7 d of exposure at  $80^{\circ}\text{C}$ : (a) SEM image of surface morphology with 100x magnification, (b) SEM image of surface morphology with 2,000x magnification, (c) XRD pattern.

phase. The fact that the point was slightly to the left of the line (in the undersaturated region) could indicate that mackinawite was gradually being converted into pyrite, although the margin was too small to be certain. The same operational point shown in Figure 21(b) was very close to the boundary for pyrite formation, confirming the XRD findings.

• **Results After 7 Days of Exposure:** The surface morphologies and composition of the corrosion product layer on the steel surface after 7 d of exposure are shown in Figure 22. The appearance was similar to the result from 4 d of exposure shown in Figure 20. The major difference was the quantities of the different iron sulfide phases. The SEM images in Figure 22 show more cubic crystals in lighter color on the steel surface compared to the previous 4-d sample, which was probably a result of the increase in the amount of the pyrite phase. The growth of the pyrite phase was proven by the quantitative analysis of the corrosion product layer presented in Table 4. Comparing with the sample after 4 d, the percentage of pyrite grew from 2.1% to 17%. This growth is significant and may suggest rapid kinetics of the growth of pyrite crystal after the nucleation. In contrast, the pyrrhotite phase is reported to nucleate quickly but grow sluggishly, which was also detected, changing from 2.6% after 4 d to 9% after 7 d. At the same time, the percentage of mackinawite decreased from 34% to 30%.

The formation of different phases of iron sulfide could be predicted with the Pourbaix diagrams generated at corresponding experimental conditions, shown in Figure 23. The experimental data point in Figure 23(a) was a little left to the boundary of mackinawite formation, which could again be indicating the transformation of mackinawite into pyrite and pyrrhotite. The experimental data point in Figure 23(b) was close to the “triple point” where all three phases (mackinawite, pyrite, and pyrrhotite) were stable, confirming XRD findings. Generally, it can be concluded that at  $80^{\circ}\text{C}$  the calculated Pourbaix diagrams are in reason-

**TABLE 4**  
XRD Quantitative Analysis of the Formed Corrosion Products Layer at 80°C

Phases	Iron	Mackinawite	Pyrrhotite	Greigite	Pyrite	Iron Carbide
After 4 d	55%	34%	2.6%	1%	2.1%	4.8%
After 7 d	39%	30%	9%	2.1%	17%	3%

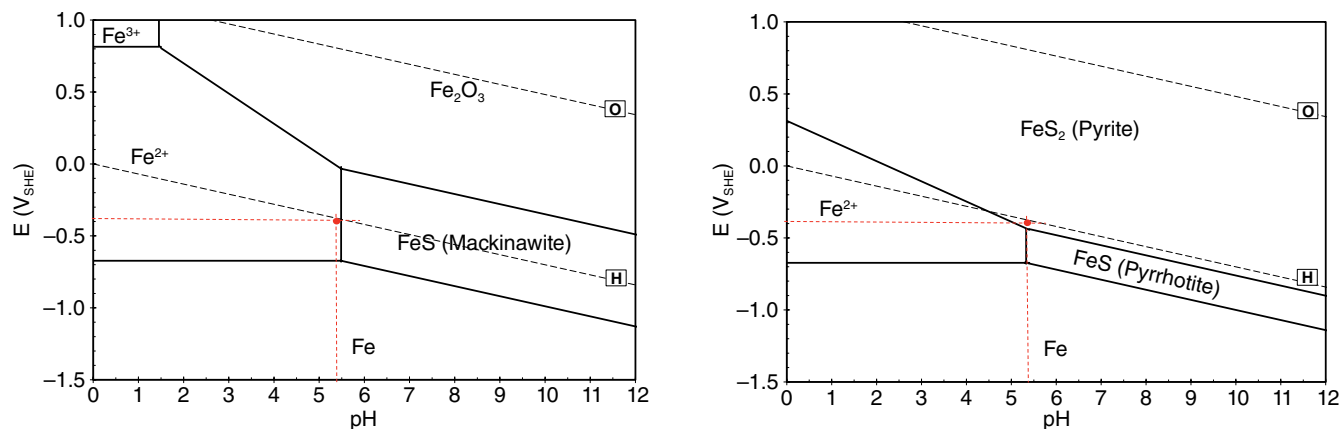


**FIGURE 23.** Verification of Pourbaix diagram after 7 d of exposure (Pourbaix diagram was generated at  $T = 80^{\circ}\text{C}$ ,  $p\text{H}_2\text{S} = 5.3 \text{ kPa}$ ,  $[\text{Fe}^{2+}] = 0.115 \text{ ppm}$ ,  $[\text{Fe}^{3+}] = 1.0 \times 10^{-6} \text{ M}$ ): (a) mackinawite, (b) mackinawite/greigite/pyrrhotite/pyrite.

able agreement with the experimental results, confirming their validity. Furthermore, Pourbaix diagrams offered complementary information to those obtained by electrochemical and analytical techniques, thereby improving our understanding of the complex evolution of the corrosion process under conditions where different iron sulfide polymorphs form.

## CONCLUSIONS

- ❖ A comprehensive thermodynamic model has been developed to predict corrosion products for an  $\text{H}_2\text{S}$ - $\text{H}_2\text{O}$ -Fe system with the focus on the conditions typical for the oil and gas applications.
- ❖ Pourbaix diagrams for an  $\text{H}_2\text{S}$ - $\text{H}_2\text{O}$ -Fe system generated by the thermodynamic model were experimentally validated. The corrosion products formed on the steel surface were predicted by the Pourbaix diagrams constructed for the experimental conditions and confirmed by XRD analysis.
- ❖ Mackinawite and pyrrhotite were detected as corrosion products in  $\text{H}_2\text{S}$  corrosion of mild steel at  $25^{\circ}\text{C}$ . Mackinawite, pyrrhotite, and pyrite were found at  $80^{\circ}\text{C}$ .

## ACKNOWLEDGMENTS

The authors would like to express sincere appreciation to the following industrial sponsors for their financial support and direction: Anadarko, Baker Hughes, BP, Chevron, Clariant Oil Services, CNPC Tubular Goods, ConocoPhillips, DNV GL, Hess, INPEX Corporation, M-I SWACO, Multi-Chem, Nalco Cham-

pion, Occidental Oil Company, Petrobras, Petroleum Development Oman, Petroleum Institute (GRC), Petronas, PTT, Saudi Aramco, Sinopec, TransCanada, TOTAL, and Wood Group Integrity Management.

The authors also appreciate the help offered at the Center for Electrochemical Engineering Research, Department of Chemical and Biomolecular Engineering at Ohio University, enabling the use of the XRD equipment. Last but not least, great thanks go to Cody Shafer for the assistance in constructing the experimental set-up figure.

## REFERENCES

1. S.N. Smith, M. Joosten, "Corrosion of Carbon Steel by  $\text{H}_2\text{S}$  in  $\text{CO}_2$  Containing Oilfield Environments," CORROSION/06, paper no. 115 (Houston, TX: NACE International, 2006).
2. Y. Zheng, B. Brown, S. Nešić, *Corrosion* 70, 4 (2014): p. 351-365.
3. W. Sun, S. Nešić, *Corrosion* 65, 5 (2009): p. 291-307.
4. A. Anderko, P. McKenzie, R.D. Young, *Corrosion* 57, 3 (2001): p. 202-213.
5. Y. Zheng, J. Ning, B. Brown, S. Nešić, *Corrosion* 71, 3 (2015): p. 316-325.
6. W. Sun, S. Nešić, S. Papavinasam, *Corrosion* 64, 7 (2008): p. 586-599.
7. E. Abelev, J. Sellberg, T.A. Ramanarayanan, S.L. Bernasek, *J. Mater. Sci.* 44 (2009): p. 6167-6181.
8. S. Kapusta, D. Raghu, J. Richards, "Managing Sour Gas Corrosion: Testing, Design, Implementation and Field Results," CORROSION 08, paper no. 641 (Houston, TX: NACE, 2008).
9. S.N. Smith, B. Brown, W. Sun, "Corrosion at Higher  $\text{H}_2\text{S}$  Concentrations and Moderate Temperatures," CORROSION 11, paper no. 081 (Houston, TX: NACE, 2011).
10. S.M. Wilhelm, "Galvanic Corrosion Caused by Corrosion Products," in *Galvanic Corrosion*, ASTM STP 978, ed. H.P. Hack, (Philadelphia, PA: American Society for Testing and Materials, 1988).
11. C.M. Menendez, V. Jovancevic, S. Ramachandran, M. Morton, D. Stegmann, *Corrosion* 69, 2 (2013): p. 145-156.
12. E.D. Verink, Jr., "Simplified Procedure for Constructing Pourbaix Diagrams," in *Uhlig's Corrosion Handbook*, 3rd ed., ed. R.W. Revie (Hoboken, NJ: John Wiley & Sons Inc., 2011), p. 93-101.

13. J. Bouet, J.P. Brenet, *Corros. Sci.* 3 (1963): p. 51-63.
14. M. Ueda, *Corros. Eng.* 44, 3 (1995): p. 159-174.
15. A. Anderko, P.J. Shuler, *Computers & Geosciences* 23, 6 (1997): p. 647-658.
16. A. Anderko, S.J. Sanders, R.D. Young, *Corrosion* 53, 1 (1997): p. 43-53.
17. R.J. Biernat, R.G. Robins, *Electrochim. Acta* 17 (1972): p. 1261-1283.
18. D.D. Macdonald, B.C. Syrett, *Corrosion* 35, 10 (1979): p. 471-475.
19. C.M. Chen, K. Aral, G.J. Theus, "Computer-Calculated Potential pH Diagrams to 300°C," Electronic Power Research Institute, EPRI NP-3137, 1983.
20. T. Tanupabrungsun, D. Young, B. Brown, S. Nešić, "Construction and Verification of Pourbaix Diagrams for CO<sub>2</sub> Corrosion of Mild Steel Valid up to 250°C," CORROSION 12, paper no. 1418 (Houston, TX: NACE, 2012).
21. E.H. Oelkers, H.C. Helgeson, E.L. Shock, D.A. Sverjensky, J.W. Johnson, V.A. Pokrovskii, *J. Phys. Chem. Ref. Data* 24, 4 (1995): p. 1401-1560.
22. M.H. Kaye, W.T. Thompson, "Computation of Pourbaix Diagrams at Elevated Temperature," in *Uhlig's Corrosion Handbook*, 3rd ed., ed. R.W. Revie (Hoboken, New Jersey: John Wiley & Sons Inc., 2011), p. 111-122.
23. J. Ning, Y. Zheng, D. Young, B. Brown, S. Nešić, *Corrosion* 70, 4 (2014): p. 375-389.
24. O. Kubaschewski, C.B. Alcock, P.J. Spencer, *Material Thermochemistry*, 6th ed. (Oxford, United Kingdom: Pergamon Press, 1993).
25. M. Binnewies, E. Milke, *Thermochemical Data of Elements and Compounds*, 2nd revised and extended ed. (Weinheim, Germany: Wiley-VCH, 2002).
26. O. Knacke, O. Kubaschewski, K. Hesselmann, *Thermochemical Properties of Inorganic Substances*, 2nd ed. (Berlin, Germany: Springer-Verlag, 1991).
27. R.A. Robie, B.S. Hemingway, J.R. Fisher, "Thermodynamic Properties of Mineral and Related Substances at 1 Bar Pressure and at Higher Temperatures," U.S. Geological Survey Bulletin 1452, 1978.
28. M.W. Chase, J.R. Downey, "NIST-JANAF Thermochemical Tables," *J. Phys. Chem. Ref. Data*, 4th ed., Monograph No. 9 (Gaithersburg, MA: NIST, 1998).
29. University of Rhode Island, reference materials, "Thermodynamic Quantities for Substances and Ions at 25°C," June 28, 2015, <http://bilbo.chm.uri.edu/CHM112/tables/thermtable.htm>.
30. Indiana University, reference materials, "Standard Thermodynamic Properties of Chemical Substances," June 28, 2015, <http://courses.chem.indiana.edu/c360/documents/thermodynamicdata.pdf>.
31. H.E. Barner, R.V. Scherman, *Handbook of Thermodynamical Data for Compounds and Aqueous Species* (New York, NY: John Wiley & Sons, 1978).
32. K.C. Mills, *Thermodynamic Data for Inorganic Sulfides, Selenides, and Tellurides* (London, United Kingdom: Butterworths, 1974).
33. B. Beverskog, I. Puigdomenech, *Corros. Sci.* 38, 12 (1996): p. 2121-2135.
34. V.B. Parker, I.L. Khodakovskii, *J. Phys. Chem. Ref. Data* 24, 5, (1995): p. 1699-1745.
35. E.E. Bernarducci, L.R. Morss, A.R. Miksztat, *J. Solution Chem.* 8 (1979): p.717.
36. E.L. Shock, H.C. Helgeson, *Geochim. Cosmochim. Acta* 52 (1988): p. 2009.
37. F. Gronvold, E.F. Westrum, Jr., *Inorg. Chem.* 1, 1 (1962): p. 36-48.
38. D.J. Vaughan, J.R. Craig, "Sulfide Thermochemistry," in *Mineral Chemistry of Metal Sulfides*, eds. W.B. Harland, S.O. Agrell, A.H. Cook, N.F. Hughes (London, United Kingdom: Cambridge University Press, 1978).
39. B. Brown, "The Influence of Sulfides on Localized Corrosion of Mild Steel" (Ph.D. diss., Ohio University, 2013).
40. D. Abayarathna, A. Naraghi, S. Wang, "The Effect of Surface Films on Corrosion of Carbon Steel in a CO<sub>2</sub>-H<sub>2</sub>S-H<sub>2</sub>O System," CORROSION/05, paper no. 624 (Houston, TX: NACE, 2005).
41. W. Sun, S. Nešić, S. Papavinasam, *Corrosion* 64, 7 (2008): p. 586-599.
42. J. Han, B. Brown, D. Young, S. Nešić, *J. Appl. Electrochem.* 40 (2010): p. 683.